

**EXPLORING VANADIUM BASED POLYANIONIC  
STRUCTURED CATHODE MATERIALS FOR HIGH  
VOLTAGE SODIUM-ION BATTERIES**

**Simranjot Kaur Sapra**



**DEPARTMENT OF PHYSICS**

**INDIAN INSTITUTE OF TECHNOLOGY DELHI**

**JULY 2025**

© Indian Institute of Technology Delhi (IITD), New Delhi, 2025

**EXPLORING VANADIUM BASED POLYANIONIC  
STRUCTURED CATHODE MATERIALS FOR HIGH  
VOLTAGE SODIUM-ION BATTERIES**

by

**Simranjot Kaur Sapra**

**DEPARTMENT OF PHYSICS**

*Submitted*

*in fulfilment of the requirements of the degree of*

*Doctor of Philosophy*

*to the*



**INDIAN INSTITUTE OF TECHNOLOGY DELHI**

**JULY 2025**

*Dedicated to ...*

*My dear parents*

***Jaswant Singh and Balwant Kaur***

*who love, bless and motivate me to work hard  
for everything I wish to achieve in life  
and have been my foundation throughout this journey.*

## DECLARATION BY THE CANDIDATE

I, **Simranjot Kaur Sapra**, declare that the work in this thesis entitled “*Exploring Vanadium based Polyanionic Structured Cathode Materials for High Voltage Sodium-ion Batteries*”, is my own work conducted under the supervision of Prof. Rajendra S. Dhaka and Prof. Jeng-Kuei Chang, approved by student research committee (SRC) at Department of Physics, Indian Institute of Technology Delhi, New Delhi, India and National Yang Ming Chiao Tung University, Hsinchu, Taiwan.

I further declare that this work is not submitted and will not be submitted to any other institute/university for any degree or diploma. I confirm the norms and guidelines provided in the ethical code of conduct by the institute. In lieu of this, I have given appropriate credit to all materials, theoretical analysis, data, figures and text used from other sources, by citing them in the text of the thesis. I also confirm that I have not used any artificial intelligence (AI) based software for writing any part of the thesis.

Signature \_\_\_\_\_

Name of the Candidate: Simranjot Kaur Sapra

Entry Number: 2018TIZ8367

Department of Physics

Indian Institute of Technology Delhi

Hauz Khas, New Delhi – 110016, India.

Date: 28 July 2025

## CERTIFICATE OF THE SUPERVISOR

This is to certify that the thesis entitled “*Exploring Vanadium based Polyanionic Structured Cathode Materials for High Voltage Sodium-ion Batteries*”, being submitted by **Simranjot Kaur Sapra** (2018TIZ8367) to the Department of Physics, Indian Institute of Technology Delhi and National Yang Ming Chiao Tung University, Taiwan under the IIT Delhi-NYCU Joint Doctoral Program, for the award of the degree of **Doctor of Philosophy** is a record of bonafide work carried out by her. She has worked under my supervision and guidance and has fulfilled the requirements for the submission of this thesis, which in my opinion has reached the requisite standard.

The results contained in this thesis have not been submitted, in part or full, to any other university or institute for the award of any degree/diploma.

Signature \_\_\_\_\_

**Prof. Rajendra S. Dhaka**

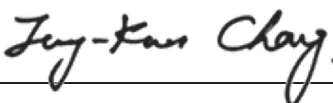
Professor

Department of Physics

Indian Institute of Technology Delhi

Hauz Khas, New Delhi – 110016, India.

Date:

Signature \_\_\_\_\_  


**Prof. Jeng-Kuei Chang**

Distinguished Professor

Department of Material Science and Engineering

International College of Semiconductor Technology

National Yang Ming Chiao Tung University

University Road, Hsinchu, Taiwan (Republic of China) – 30010.

Date:

# ACKNOWLEDGEMENTS

Foremost, I attribute the successful completion of Ph.D. voyage to the Almighty God for bestowing me with endless blessings, unwavering strength, well-being, wisdom and resilience essential for achieving this objective and bring it to fruition.

I would like to express my sincere appreciation to my esteemed thesis advisors, Prof. Rajendra S. Dhaka and Prof. Jeng-Kuei Chang, whose invaluable guidance greatly influenced the trajectory of my doctoral studies. Their benoalent mentorship, continual encouragement, unwavering support, dedicated efforts and profound scientific expertise provide me with fertile ground where I could acquire wisdom, knowledge and intellectual freedom, ultimately leading to the successful completion of my thesis. I wish to particularly acknowledge Prof. Rajendra S. Dhaka for his cooperation, consistent support, perceptive encouragement, insightful advice and instilling me the values of commitment to research, persistence, diligence, discipline and punctuality throughout my Ph.D. journey. I also wish to sincerely thank Prof. Jeng-Kuei Chang at NYCU, whose dedicated efforts, continuous support, insightful feedback, encouragement and scientific expertise were a blessing during the arduous journey of doctoral work. I sincerely thank both of them for granting me the incredible opportunity to be part of their research groups and for providing the infrastructure necessary for my research endeavor.

I wish to convey my sincere thanks to my Student Research Committee (SRC) members at Indian Institute of Technology Delhi: Prof. Neeraj Khare, Prof. Rajendra Singh and Prof. Amit Gupta, for their valuable suggestions during the Semester Progress Presentations. I am also thankful to Dr. Mir Wasim Raja and Mononita Das at the CSIR-Central Glass & Ceramic Research Institute (Kolkata) for the fruitful collaboration.

I sincerely thank the Ministry of Human Resource Development (MHRD) and the International College of Semiconductor Technology, National Yang-Ming Chiao Tung University for the financial assistance and Senior Research Fellowship, which facilitated my undertaking of this expedition. I express my profound gratitude to Micron Technology Taiwan, Inc. for awarding me the “Micron Scholarship for Women in STEM,” which enabled me to carry out this research work. I acknowledge the Department of Science and Technology, Government of India, for financial support through “DST-IIT Delhi Energy Storage Platform on Batteries” (project no. DST/TMD/MECSP/2K17/07). I deeply thank the National Science and Technology Council (NSTC), Taiwan for the funding support. I acknowledge SERB-DST for the core research grant (file no.: CRG/2020/003436). I extend thanks to Department of Physics and Central Research Facility, IIT Delhi for providing the research facilities for completion of thesis work.

I consider myself privileged to be associated with the Novel Materials and Interface Physics Laboratory (NMIPL), renowned for its rich research history and commitment to innovation. I express my appreciation to my former and current lab colleagues: Dr. Mahesh Chandra, Dr. Priyanka, Dr. Rishabh Shukla, Dr. Ajay Kumar, Dr. Pravin Dwivedi, Dr. Hari Raj, Dr. Sandeep Soundryal, Dr. P Senthilkumar, Dr. Rupesh Tiwari, Dr. Ramcharan Meena, Dr. Jayjit Mukherjee, Dr. Gurudutt Gupta, Dr. Shivangi Rajput, Jayashree Pati, Manish Kr. Singh, Sudhanshu Gupta, Madhav Sharma, Priyanka Yadav, Riya Gulati, Pooja Sindhu, Kavita and Komal, who became my second family during this journey. I am especially grateful to Dr. Rishabh Shukla, Dr. Ajay Kumar and Dr. Pravin Dwivedi, for their unwavering support and encouraging discussions during the challenging phases of my experimental work. I extend my heartfelt thanks to Manish Kr. Singh for his immense help during the experimental work. I am grateful to Jayashree Pati, Riya Gulati and Manish Kr. Singh for their valuable time and efforts for the XRD measurements. I wish to gratefully acknowledge my friends at IIT Delhi: Dr. Pallavi Aggarwal, Dr. Pallabi Parui, Dr. Manjari Jain, Dr. Sakshi Tanwar, Dr. Monika, Sushila Dhaka and Dr. Sumana Bandhopadhyay who motivated me to pursue my research interests. I would like to acknowledge my friends outside IIT Delhi: Sonali Khanna, Superv Jain, Rupamjeet Singh Gill and Vishal Sharma. I am extremely grateful to my colleagues at NYCU, particularly: Luke, Ryan, Jen, Dita, Rupan, Andy, Danny, Jasmine, Sandra and Ananya for their unwavering support, friendship and encouragement. I extend my sincere thanks to Dr. Bharath Umesh, Dr. Diah Augistana Puspatisiri, Dr. Purna Chandra Rath, Dr. Jagabandhu Patra and Dr. R. F. H. Hernandha for their valuable scientific discussions. I am thankful to Ms. Janet Chen and Ms. Yiting Lin for their immense assistance in the official documentation at NYCU.

I am elated to express my heartfelt gratitude to my family members for their unending love and support, motivation, understanding and blessings. I am profoundly grateful to my parents, Jaswant Singh and Balwant Kaur, brother Arshdeep Singh Sapra, sister-in-law Sandeep Kaur, sister Amanpreet Kaur Bhatti, brother-in-law Bikramjeet Singh Bhatti, nephew Manraj Singh Bhatti, and my extended family members for their tremendous support throughout my academic and personal journey. The successful completion of my doctoral thesis would have been merely an aspiration without the significant contributions and support of everyone who created an environment favorable to my academic endeavors. I am grateful to all who were instrumental in cultivating the encouraging atmosphere that enabled me to carry out my research over the years.

*“The expert at anything was once a beginner.”—Helen Hayes*

*Simranjot Kaur Sapra*



# ABSTRACT

Sustainable and efficient energy storage devices are crucial to meet the soaring global energy demand. In this context, Na-ion batteries (SIBs) have emerged as forerunner technologies in the energy storage sector, attributed to the abundant resources, wide availability, and cost-effectiveness of required raw materials. In recent years, a lot of research is being conducted on the development of sodium-based electrode materials and electrolytes, considering the similar intercalation chemistry and structural properties with lithium battery technology. However, the exploration of high energy density electrodes with long cycle life and excellent rate performance remains censorious, owing to the larger ionic radius (1.02 Å for Na vs. 0.76 Å for Li). Therefore, the large-scale production of SIBs seeks attention to bring them into the commercial layout for practical where the structural and electrochemical stability of cathode materials play a crucial role for high energy density. Recently, polyanionic compounds have been explored as potential candidates owing to their great thermal and chemical stability, high redox potential and rich structural diversity. The main focus of this thesis is the comprehensive investigation of the physical and electrochemical properties of the phosphate based polyanionic cathodes for SIBs.

In this line,  $\text{Na}_3\text{V}_2(\text{PO}_4)_3$ , also known as Na-ion SuperIonic CONductor (NASICON) based polyanionics are widely explored as the pertinent cathode materials in sodium-ion batteries due to their 3D open framework, which can accommodate a wide range of Na content and can offer high ionic conductivity with great structural stability. However, owing to the inferior electronic conductivity, these materials suffer from unappealing rate capability and cyclic stability for practical applications. Therefore, the investigation of the effect of Co substitution at V site on the electrochemical performance and diffusion kinetics of  $\text{Na}_3\text{V}_{2-x}\text{Co}_x(\text{PO}_4)_3/\text{C}$  ( $x = 0-0.15$ ) cathodes has been conducted. All the samples are characterized through Rietveld refinement of the x-ray diffraction patterns, Raman spectroscopy, transmission electron microscopy, etc. The improved electrochemical performance for the  $x = 0.05$  electrode with reversible capacity of  $105 \text{ mAh g}^{-1}$  at  $0.1 \text{ C}$  has been observed. Interestingly, the specific capacity of  $80 \text{ mAh g}^{-1}$  is achieved at  $10 \text{ C}$  with retention of about 92% after 500 cycles and 79.5% after 1500 cycles and having nearly 100% Coulombic efficiency. The extracted diffusion coefficient values through galvanostatic intermittent titration technique (GITT) and cyclic voltammetry (CV) are found to be in the range of  $10^{-9}-10^{-11} \text{ cm}^2 \text{ s}^{-1}$ . The postmortem studies show the excellent structural and morphological stability after testing for 500 cycles at  $10 \text{ C}$ .

Furthermore, one  $\text{PO}_4^{3-}$  group has been replaced by three  $\text{F}^-$  ions in  $\text{Na}_3\text{V}_2(\text{PO}_4)_3$  to raise the operating potential, originating from the inductive effect. The storage mechanism and diffusion kinetics of  $\text{Na}_3\text{V}_{2-x}\text{Ni}_x(\text{PO}_4)_2\text{F}_3/\text{C}$  ( $x = 0-0.07$ ) cathodes

are investigated through electrochemical impedance spectroscopy (EIS), GITT and CV measurements. All the samples are prepared through the facile pH-assisted sol-gel route and crystallize in the  $P4_2/mnm$  symmetry. The optimal doping of Ni ( $x = 0.05$ ) exhibits superior specific capacities of 119 and 100 mAh g<sup>-1</sup> at 0.1 C and 10 C rates, respectively, along the excellent capacity retention of 78% after 2000 cycles at 10 C rate with nearly 100% Coulombic efficiency. The apparent diffusion coefficient values are found to be in the range of 10<sup>-9</sup>-10<sup>-10</sup> cm<sup>2</sup> s<sup>-1</sup> through detailed analysis of CV and GITT. Moreover, we report the reversible structural evolution and morphological changes during charging and discharging under non-equilibrium conditions through the *operando* X-ray diffraction and the *in-situ* synchrotron-based transmission X-ray microscopy, respectively. Further, to understand the stability mechanism and obtain precise polarization values, we performed the distribution of relaxation times (DRT) analysis using the EIS data. The structure and morphology are found to be stable after long cycling.

Furthermore, cellulose-based paper separators are employed in SIBs as a viable and economical substitute for conventional separators, owing to their sustainability, scalability, safety and cost-effectiveness. These paper-based multilayer separators provide desirable characteristics such as excellent electrolyte wettability, thermal stability, and ionic conductivity, which are essential for the efficient operation of SIBs. In this investigation, the cellulose separator is coated by a layer of polyvinylidene fluoride polymer, followed by a second layer of BaTiO<sub>3</sub> particles impregnated in styrene butadiene rubber polymer. The final lamination is performed by the styrene butadiene rubber in varying concentrations (0.05, 0.75, and 1.0 w/v%). The incorporated polymer matrices improve the flexibility, adhesion and dispersion of the nanoparticles and affinity of the electrolyte to the electrode. The BaTiO<sub>3</sub> is a ferroelectric filler improves the conduction mechanism of Na<sup>+</sup> ions, which is also confirmed by the bulk ionic conductivity measurements. Herein, x-ray diffraction and Fourier transform infrared spectroscopy are employed to verify the structure of the paper separators. The morphology of the paper separators is observed through a field emission scanning electron microscope, which shows the uniform interconnected fibers with the porous structure. The galvanostatic charge-discharge profiles show improved electrochemical performance with the Na<sub>3</sub>V<sub>2</sub>(PO<sub>4</sub>)<sub>3</sub> and hard carbon electrodes for 0.75 w/v% SBR content, during full cell cycling. The designed separators with 0.75 w/v% content of styrene butadiene rubber exhibit good capacity retentions of 62 % with nearly 100 % coulombic efficiency when cycled for 200 cycles at 0.5 C rate, compared to the other two separators. Furthermore, these separators demonstrate enhanced ionic conductivity as temperatures increase, providing additional evidence of their excellent thermal stability. Pre- and post-electrochemical impedance spectroscopy measurements show decreased interfacial resistances at 0.75 w/v% styrene butadiene rubber compared to other concentrations.

Further, the electrolyte leakage and flammability poses serious safety concerns in battery industry. Interestingly, Solid-state sodium-ion batteries are promising alternatives for safe, high voltage and high-density batteries. In this direction, the liquid electrolytes are replaced by the composite polymer solid electrolytes, also known as quasi-solid electrolytes. Here, the polymer matrix comprises of poly(vinylidene fluoride-co-hexafluoropropylene) (PVDF-HFP) and polypropylene carbonate (PPC) copolymers (8:2), which possess high dielectric constant, prominent mechanical strength, high thermal stability and the great flexibility. The Na-ions move across the polymer matrices, while ceramic particles ( $\text{Na}_{1+x}\text{Zr}_2\text{P}_{3-x}\text{Si}_x\text{O}_{12}$  ( $x=2$  for NZSP)) are impregnated to improve the polymer-ceramic interactions and electrode/electrolyte interface to withstand the volume changes upon cycling. The high-temperature sintering at  $1100^\circ\text{C}$  prepares NZSP inorganic material to have sufficient conductivity for ion transport. Furthermore, to provide additional  $\text{Na}^+$  ion pathways and enhance ionic conductivity, ionic liquids (N-propyl-N-methylpyrrolidinium bis(fluorosulfonyl)imide, N-propyl-N-methylpyrrolidinium bis(trifluoromethanesulfonyl), 1-Ethyl-1-methylimidazolium bis(fluorosulfonyl)imide) and organic solvent (Succinonitrile) are employed as plasticizers in above polymer-ceramic complex. The effect of the plasticizers on the NVPF cathode in half-cell configurations is studied using X-ray diffraction, infrared spectroscopy, cross section field emission scanning electron microscopy and electrochemical measurements. Interestingly, these composite polymer electrolytes are stable up to 4.5 V, as confirmed from the linear sweep voltammetry measurements. It was found that 1-Ethyl-1-methylimidazolium bis(fluorosulfonyl)imide ionic liquid showed the best performance in comparison to other plasticizers, owing to its high ionic conductivity and excellent stability and capacity retention after 100 cycles at 0.5 C.

Overall, a systematic investigation of the polyanionic cathodes, paper separators and composite solid electrolytes has been conducted in the present thesis. The design and optimization of the structural properties of the proposed materials in combination with the physical and electrochemical property correlation in sodium-ion cells has led to the identification of novel high voltage cathode materials with superior electrochemical performance. The development of solid state electrolytes with the polyanionic cathodes is expected to provide a pathway for the safe, low cost, long cycle life and high energy density batteries for large-scale stationary applications. Notably, the comprehensive study of cathodes, separators and electrolytes can be employed to further engineer and grab a better understanding of the physical and electrochemical properties for efficient battery performance.

## सारांश

सतत और कुशल ऊर्जा भंडारण उपकरण बढ़ती वैश्विक ऊर्जा मांग को पूरा करने के लिए अत्यंत आवश्यक हैं। इस संदर्भ में, सोडियम आयन बैटरियाँ (SIBs) ऊर्जा भंडारण क्षेत्र में एक प्रमुख तकनीक के रूप में उभरी हैं, जिसका श्रेय आवश्यक कच्चे माल की प्रचुरता, व्यापक उपलब्धता और किफायती लागत को जाता है। हाल के वर्षों में, लिथियम बैटरी तकनीक के समान अंतर्निवेश रसायन और संरचनात्मक गुणों को ध्यान में रखते हुए, सोडियम-आधारित इलेक्ट्रोड सामग्री और इलेक्ट्रोलाइट्स के विकास पर काफी शोध किया जा रहा है। हालाँकि, उच्च ऊर्जा घनत्व वाले इलेक्ट्रोड्स की खोज, जो लंबी चक्र जीवन और उत्कृष्ट दर क्षमता प्रदान करें, चुनौतीपूर्ण बनी हुई है, क्योंकि सोडियम आयन का आयनिक त्रिज्या (1.02 Å) लिथियम (0.76 Å) की तुलना में बड़ा होता है। अतः SIBs का बड़े पैमाने पर उत्पादन उन्हें व्यावसायिक उपयोग में लाने के लिए आवश्यक है, जिसमें उच्च ऊर्जा घनत्व प्राप्त करने हेतु कैथोड सामग्रियों की संरचनात्मक और विद्युत-रासायनिक स्थिरता प्रमुख भूमिका निभाती है। हाल ही में, बहु ऋणायनिक यौगिकों को संभावित विकल्पों के रूप में परीक्षण किया गया है क्योंकि इनमें उच्च तापीय एवं रासायनिक स्थिरता, उच्च रिडॉक्स विभव और समृद्ध संरचनात्मक विविधता विद्यमान है। प्रस्तुत शोधकार्य का मुख्य उद्देश्य SIBs के लिए फॉस्फेट आधारित, बहु ऋणायनिक कैथोड्स के भौतिक और विद्युत रासायनिक प्रदर्शन की विस्तृत जाँच करना है।

इस संदर्भ में,  $\text{Na}_3\text{V}_2(\text{PO}_4)_3$ , जिसे सोडियम आयन सुपरआयोनिक कंडक्टर (NASICON) के रूप में भी जाना जाता है, आधारित पॉलीऐनायोनिक यौगिकों को सोडियम-आयन बैटरियों में उपयुक्त कैथोड सामग्री के रूप में व्यापक रूप से खोजा गया है। इसका कारण इसका त्रि-आयामी उद्घाटित संरचना है, जो सोडियम आयनों की एक विस्तृत सीमा को समाहित कर सकता है और उच्च आयनिक चालकता के साथ-साथ उत्कृष्ट संरचनात्मक स्थिरता प्रदान करता है। हालांकि, कमजोर विद्युतकणीय चालकता के कारण, ये दर क्षमता और चक्र स्थिरता के दृष्टिकोण से व्यावहारिक अनुप्रयोगों में कमजोर प्रमाणित होती हैं। इसलिए,  $\text{Na}_3\text{V}_{2-x}\text{Co}_x(\text{PO}_4)_3/\text{C}$  (जहाँ  $x=0-0.15$ ) कैथोड सामग्री में V स्थान पर Co प्रतिस्थापन का विद्युत-रासायनिक प्रदर्शन और आपेक्षिकीय गतिकी पर क्या प्रभाव पड़ता है, इसका अध्ययन किया गया है। सभी नमूनों की एक्स-रे विवर्तन प्रतिरूप की रीटवेल्ड परिष्करण, रमन विवर्तन वर्णक्रमिकी, ट्रांसमिशन इलेक्ट्रॉन माइक्रोस्कोपी आदि तकनीकों से संरचनात्मक जांच की गई। दिलचस्प रूप से, 10 C दर पर 80 mAh g<sup>-1</sup> की विशिष्ट क्षमता दर्ज की गई, जिसमें 500 चक्रों के बाद लगभग 92% क्षमता प्रतिधारण और 1500 चक्रों के बाद 79.5% क्षमता प्रतिधारण रहा, और यह लगभग 100% कुलॉम्बिक दक्षता के साथ प्राप्त हुआ। गैल्वेनोस्टैटिक इंटरमिटेंट टाइट्रेशन तकनीक (GITT) और साइक्लिक वोल्टामेट्री (CV) के माध्यम से निकाले गए विसरण गुणांक के मान 10<sup>-9</sup>-10<sup>-11</sup> सेमी<sup>2</sup>/सेकंड की सीमा में पाए गए। पश्च-परीक्षण अध्ययन से यह पता चला कि 10 C धारा घनत्व पर 500 चक्रों के बाद भी सामग्री की संरचना और आकार में उत्कृष्ट स्थिरता बनी रहती है।

इसके अतिरिक्त,  $\text{Na}_3\text{V}_2(\text{PO}_4)_3$  में एक  $\text{PO}_4^{3-}$  समूह को तीन F आयनों से प्रतिस्थापित किया गया है ताकि प्रचालन वोल्टेज को इंडक्टिव प्रभाव के कारण बढ़ाया जा सके।  $\text{Na}_3\text{V}_{2-x}\text{Ni}_x(\text{PO}_4)_2\text{F}_3/\text{C}$  ( $x=0-0.07$ ) कैथोड्स

की भंडारण प्रक्रिया और विसरण गतिकी को विद्युत रासायनिक इम्पीडेंस स्पेक्ट्रोस्कोपी (EIS), GITT, और CV मापन के माध्यम से जांचा गया है। सभी नमूनों को सरल pH-असिस्टेड सॉल-जेल विधि से तैयार किया गया और ये P4<sub>2</sub>/mnm क्रिस्टल संरचना में स्फटिकीकृत हुए। x = 0.05 के निकेल (Ni) का अनुकूल सम्मिश्रण के साथ 0.1 C और 10 C दरों पर क्रमशः 119 और 100 mAh g<sup>-1</sup> की उच्च विशिष्ट क्षमताएँ प्राप्त हुईं। इसके अतिरिक्त, 10 C दर पर 2000 चक्रों के बाद 78% क्षमता प्रतिधारण और लगभग 100% कुलॉम्बिक दक्षता प्राप्त हुई। CV और GITT के विस्तृत विश्लेषण से स्पष्ट विसरण गुणांक के मान 10<sup>-9</sup>-10<sup>-10</sup> सेमी<sup>2</sup>/सेकंड की सीमा में पाए गए। साथ ही, हमने ऑपेरेण्डो एक्स-रे विवर्तन और इन-सिटू सिन्क्रोट्रॉन-आधारित ट्रांसमिशन एक्स-रे माइक्रोस्कोपी के माध्यम से चार्जिंग और डिस्चार्जिंग के दौरान की संरचनात्मक एवं रूपात्मक परिवर्तनों का अध्ययन किया। इसके अतिरिक्त, स्थिरता की कार्यविधि को समझने तथा ध्रुवण के सटीक मान प्राप्त करने हेतु, EIS डेटा के आधार पर विश्रांति समय वितरण (DRT) का विश्लेषण किया गया। इन सभी अध्ययनों से यह ज्ञात हुआ कि लंबे चक्रों के बाद भी सामग्री की संरचना और आकार में स्थिरता बनी रहती है।

इसके अतिरिक्त, सेलुलोज-आधारित पेपर सेपरेटरों का उपयोग SIBs में पारंपरिक सेपरेटरों के एक व्यावहारिक और किफायती विकल्प के रूप में किया जा रहा है। इन सेपरेटरों में सततता, मापनीयता, सुरक्षा और कम लागत जैसे गुण विद्यमान होते हैं, जो इन्हें ऊर्जा भंडारण के लिए उपयुक्त बनाते हैं। ये पेपर-आधारित बहुपरत सेपरेटर उत्कृष्ट इलेक्ट्रोलाइट अवशोषण क्षमता, उच्च तापीय स्थिरता और बेहतर आयनिक चालकता प्रदान करते हैं, जो SIBs के कुशल संचालन हेतु आवश्यक हैं। अध्ययन के अंतर्गत, सेलुलोज सेपरेटर की सतह पर सबसे पहले पॉलीविनिलिडीन फ्लोराइड (PVDF) की परत चढ़ाई गई, जिसके पश्चात स्टाइरीन-ब्यूटाडीन रबर (SBR) पॉलीमर में मिश्रित BaTiO<sub>3</sub> कणों की दूसरी परत लगाई गई। अंतिम लेमिनेशन स्टाइरीन-ब्यूटाडीन रबर की विभिन्न सांद्रताओं (0.05%, 0.75%, और 1.0% w/v) से किया गया। इस बहुपरत संरचना के परिणामस्वरूप सेपरेटर में बेहतर लचीलापन, चिपकाव क्षमता, नैनोकणों का सम्यक् वितरण तथा इलेक्ट्रोलाइट के प्रति इलेक्ट्रोड का आकर्षण बढ़ा। BaTiO<sub>3</sub>, एक फेरोइलेक्ट्रिक भराव के रूप में, Na<sup>+</sup> आयनों के प्रवाह तंत्र को सशक्त करता है, जिसकी पुष्टि थोक आयनिक चालकता मापनों द्वारा की गई। X-ray विवर्तन (XRD) और फूरियर ट्रांसफॉर्म इन्फ्रारेड स्पेक्ट्रोस्कोपी (FTIR) के माध्यम से सेपरेटर की संरचना की पुष्टि की गई, जबकि फील्ड एमिशन स्कैनिंग इलेक्ट्रॉन माइक्रोस्कोपी (FESEM) से यह ज्ञात हुआ कि इन सेपरेटरों में एकसमान तंतुजाल और छिद्रयुक्त संरचना विद्यमान है। गैल्वेनोस्टैटिक चार्ज-डिस्चार्ज परीक्षणों में 0.75% SBR सामग्री वाले सेपरेटर ने Na<sub>3</sub>V<sub>2</sub>(PO<sub>4</sub>)<sub>3</sub> और हार्ड कार्बन इलेक्ट्रोड्स के साथ पूर्ण-सेल साइक्लिंग के दौरान अत्युत्तम इलेक्ट्रोकेमिकल प्रदर्शन दिखाया। इस संयोजन ने 0.5 C दर पर 200 चक्रों के पश्चात् 62% क्षमता प्रतिधारण और लगभग 100% कुलॉम्बिक दक्षता प्रदर्शित की, जो अन्य दोनों सेपरेटरों की तुलना में श्रेष्ठ रही। साथ ही, तापमान में वृद्धि के साथ इन सेपरेटरों की आयनिक चालकता में भी सुधार देखा गया, जो इनकी उच्च तापीय स्थिरता को सिद्ध करता है। EIS के पूर्व व पश्च परीक्षणों से यह ज्ञात हुआ कि 0.75% SBR सामग्री पर अंतरापृष्ठीय प्रतिरोध न्यूनतम होता है।

ठोस द्रवावस्था वाली SIBs उच्च वोल्टेज और घनत्व के साथ एक सुरक्षित विकल्प प्रदान करती हैं। इस दिशा में, तरल इलेक्ट्रोलाइट्स के स्थान पर क्वासी-सॉलिड या कॉम्पोज़िट पॉलीमर ठोस इलेक्ट्रोलाइट्स का उपयोग किया गया है। इस पॉलीमर मैट्रिक्स में पॉली(विनाइलिडीन फ्लोराइड-को-हेक्साफ्लोरोप्रोपिलीन (PVDF-HFP) और पॉलीप्रोपिलीन कार्बोनेट (PPC) (8:2 अनुपात में) सम्मिलित हैं, जो उच्च डायलेक्ट्रिक स्थिरांक, यांत्रिक दृढ़ता, तापीय स्थिरता और लचीलापन प्रदान करते हैं।  $\text{Na}^+$  आयनों का संचरण इस पॉलीमर संरचना के मध्य से होता है, जबकि  $\text{Na}_{1+x}\text{Zr}_2\text{Si}_x\text{P}_{3-x}\text{O}_{12}$  ( $x = 2$ , NZSP) जैसे सिरैमिक कणों को सम्मिलित कर पॉलीमर-सिरैमिक की पारस्परिक क्रिया और इलेक्ट्रोड/इलेक्ट्रोलाइट अंतरापृष्ठ को सुदृढ़ किया गया है, जिससे चक्रों के दौरान उत्पन्न आयतन परिवर्तन को सहन किया जा सके।  $1100^\circ\text{C}$  पर सिन्ट्रिंग प्रक्रिया द्वारा NZSP का निर्माण कर उसमें आयनिक संचरण के लिए पर्याप्त चालकता प्राप्त की गई।  $\text{Na}^+$  आयनों के वैकल्पिक मार्गों की उपलब्धता तथा चालकता में वृद्धि हेतु आयनिक तरल पदार्थों का प्लास्टिसाइज़र के रूप में उपयोग किया गया, जिनमें N-प्रोपाइल-N-मेथाइलपाइरोलिडिनियम बिस(फ्लोरोसल्फोनिल)इमाइड, N-प्रोपाइल-N-मेथाइलपाइरोलिडिनियम बिस(ट्राइफ्लोरोमीथेनसल्फोनिल), 1-एथाइल-1-मेथाइलइमिडाजोलियम बिस(फ्लोरोसल्फोनिल)इमाइड, तथा एक कार्बनिक विलायक-सक्सिनिट्राइल सम्मिलित हैं। इन प्लास्टिसाइज़रों के NVPF कैथोड पर प्रभाव का मूल्यांकन XRD, FTIR, FESEM तथा विद्युत-रासायनिक परीक्षणों के माध्यम से किया गया। रेखीय स्वीप वोल्टमेट्री द्वारा यह प्रमाणित हुआ कि ये संयोजित पॉलीमर इलेक्ट्रोलाइट्स 4.5 वोल्ट तक विद्युत रूप से स्थिर रहते हैं। विशेष रूप से, 1-एथाइल-1-मेथाइलइमिडाजोलियम बिस(फ्लोरोसल्फोनिल) इमाइड ने सर्वश्रेष्ठ प्रदर्शन किया, क्योंकि इस तरल में उच्च आयनिक चालकता, उत्कृष्ट संरचनात्मक स्थिरता, तथा 100 चक्रों के उपरांत  $0.5\text{ C}$  की दर पर विशिष्ट क्षमता का प्रभावी प्रतिधारण दर्ज किया गया।

समग्र रूप से, इस शोधकार्य में बहु-ऋणायनिक कैथोड, सेलुलोज़ आधारित पेपर सेपरेटर तथा संयोजित ठोस इलेक्ट्रोलाइट्स का गहन एवं व्यवस्थित परीक्षण किया गया। प्रस्तुत सामग्रियों की संरचनात्मक रूपरेखा के डिज़ाइन व अनुकूलन और उनके भौतिक व वैद्युत-रासायनिक गुणों के अंतर्संबंधों का विश्लेषण करते हुए उच्च विभव वाले नवीन कैथोड्स की पहचान की गई, जिनमें उत्कृष्ट इलेक्ट्रोकेमिकल प्रदर्शन क्षमता है। ठोस द्रवावस्था वाले इलेक्ट्रोलाइट्स के साथ इन कैथोड्स का संयोजन, विशेष रूप से स्थिर ऊर्जा आवश्यकताओं हेतु, सुरक्षित, सस्ती, दीर्घकालिक और उच्च ऊर्जा घनत्व वाली बैटरियों के विकास हेतु एक संभावनाशील मार्ग प्रशस्त करता है। यह समग्र अध्ययन बैटरी प्रणालियों की अभिकल्पना, अनुकूलन तथा गुणात्मक सुधार के लिए अत्यंत उपयोगी सिद्ध हो सकता है।

# Contents

Declaration by the Candidate	ii
Certificate of the Supervisor	iii
Acknowledgement	iv
Abstract	vii
List of Figures	xiii
List of Tables	xxi
<b>1 Introduction</b>	<b>1</b>
1.1 Introduction	2
1.2 Operation Principle of Sodium-ion Batteries	3
1.2.1 Energy Perspective of Sodium-ion Batteries	5
1.2.2 Brief Outline of Electrode–Electrolyte Interface	7
1.3 Selection of Cathodes for Sodium-ion Batteries	8
1.3.1 Polyanionic Materials as Cathodes for Sodium-ion Batteries	10
1.3.1.1 Inductive Effect in Polyanionic Compounds	11
1.3.2 Rationale for Adopting Vanadium-based Polyanionic compounds	12
1.3.2.1 Historical Context of Vanadium based Phosphates and Fluorophosphates	13
1.4 Selection of the Separators for Sodium-ion Batteries	21
1.5 Selection of the Electrolytes for Sodium-ion Batteries	24
1.5.1 Liquid Electrolytes	24
1.5.2 Solid–State Sodium-ion Electrolytes	27
1.5.3 Mechanism of Ion Transport in Solid Electrolytes	28
1.6 Investigation of the Anodes and Full cells for Sodium-ion Batteries	31
1.7 Scope of this work	33
1.8 Structure of the Thesis	35
<b>2 Experimental Methods</b>	<b>56</b>
2.1 Synthesis Routes	57

2.1.1	Solid-State Method . . . . .	57
2.1.2	Sol-gel method . . . . .	59
2.1.3	Solution Casting Method for Polymer Membranes . . . . .	61
2.2	Material Characterization . . . . .	62
2.2.1	Electron Microscopy . . . . .	62
2.2.1.1	Field Emission Scanning Electron Microscopy . . . . .	63
2.2.1.2	Transmission Electron Microscopy . . . . .	65
2.2.2	Raman Spectroscopy . . . . .	66
2.2.3	Fourier Transform Infrared Spectroscopy . . . . .	68
2.2.4	Inductively Coupled Plasma Optical Emission Spectroscopy . . . . .	69
2.2.5	Dynamic Light Scattering . . . . .	70
2.2.6	X-ray Diffraction . . . . .	71
2.2.7	X-ray Photoelectron Spectroscopy . . . . .	74
2.2.8	Transmission X-ray Microscopy . . . . .	76
2.3	Electrode Fabrication and Coin-cell Assembly . . . . .	77
2.4	Electrochemical Characterization . . . . .	79
2.4.1	Galvanostatic Charge and Discharge Measurements . . . . .	79
2.4.2	Galvanostatic Intermittent Titration Technique . . . . .	82
2.4.3	Electrochemical Impedance Spectroscopy . . . . .	84
2.4.4	Cyclic Voltammetry . . . . .	87
2.4.5	Faradaic Charge Storage . . . . .	90
2.4.5.1	Pseudocapacitance . . . . .	90
2.4.5.2	Battery-Type Mechanisms . . . . .	91
2.4.6	Capacitive Charge Storage . . . . .	91
2.4.6.1	Power Law Analysis ( $i = av^b$ ) . . . . .	91
2.4.6.2	Current Deconvolution . . . . .	92
<b>3</b>	<b>Improved electrochemical performance of NASICON type <math>\text{Na}_3\text{V}_{2-x}\text{Co}_x(\text{PO}_4)_3/\text{C}</math> (<math>x = 0-0.15</math>) cathode for high rate and stable sodium-ion batteries</b>	<b>97</b>
3.1	Introduction . . . . .	98
3.2	Experimental Section . . . . .	99
3.3	Results and discussion . . . . .	102
3.4	Conclusion . . . . .	120
<b>4</b>	<b>Delineating the role of <math>\text{Ni}^{2+}</math> Substitution in <math>\text{Na}_3\text{V}_2(\text{PO}_4)_2\text{F}_3</math> Cathodes for High Voltage Sodium-Ion Batteries</b>	<b>128</b>
4.1	Introduction . . . . .	129
4.2	Experimental Section . . . . .	131
4.3	Results and discussion . . . . .	133
4.3.1	Crystal and electronic structures, morphology and microstructure with elemental mapping . . . . .	133
4.3.2	Electrochemical Performance and diffusion kinetics . . . . .	141
4.3.3	<i>Operando</i> XRD measurements . . . . .	147
4.3.4	Distribution of Relaxation Times (DRT) Analysis . . . . .	152
4.3.5	Post-cycling <i>ex-situ</i> XRD and SEM measurements . . . . .	155
4.4	Conclusions . . . . .	156

---

<b>5</b>	<b>Investigating the electrochemical performance of sustainable trilayer coated cellulose-based paper separators in sodium-ion batteries</b>	<b>165</b>
5.1	Introduction . . . . .	166
5.2	Experimental Section . . . . .	168
5.3	Results and discussion . . . . .	170
5.3.1	Physical Characterizations . . . . .	170
5.3.2	Impedance Spectroscopy . . . . .	178
5.3.3	Electrochemical performance of full cells . . . . .	182
5.4	Conclusions . . . . .	190
<b>6</b>	<b>Filler Integrated Plasticized Composite Polymer Solid Electrolytes for Solid State Sodium-Ion Batteries</b>	<b>198</b>
6.1	Introduction . . . . .	199
6.2	Experimental Section . . . . .	201
6.3	Results and discussion . . . . .	203
6.4	Conclusion . . . . .	214
<b>7</b>	<b>Conclusion and Future Scope of Research</b>	<b>221</b>
	<b>Publications</b>	<b>225</b>
	<b>Conferences and Presentations</b>	<b>225</b>
	<b>Biodata</b>	<b>228</b>

# List of Figures

1.1	(a) An overview of energy devices being employed for the portable electronics and large scale energy storage in electric vehicles and (b) the life cycle assessment (LCA) parameters of the batteries. Adapted from ref. [1,2].	3
1.2	(a) The distribution of Li resources in world; (b) the abundance of elements in the earth's crust; (c) the comparison of physical properties of $\text{Na}^+$ and $\text{Li}^+$ ; (d) the applications of the Na-ion battery power system. Adapted from ref. [8].	4
1.3	(a) Working principle of Na-ion insertion/de-insertion in SIBs, and the relative energy of the chemical potentials $\mu_A$ , $\mu_C$ and $E_g$ for open-circuit with (b) liquid electrolyte and (c) solid electrolyte [17].	6
1.4	(a) The tree classification of cathode materials for SIBs with one branch corresponding to division of family of polyanionic compounds [17] and (b) Operating potential and capacity of recently studied polyanionic compounds, Adapted from ref. [34].	9
1.5	(a) Energy level diagram for the ionic and covalent bonds [17], (b) Charge localization of the ionic bond around $\text{XO}_4$ tetrahedra, Adapted from ref. [13] and (c) Electronegativity values of B, P, Si and S elements, as on Pauling scale.	10
1.6	The vanadium environments with various oxidation states and number in the square bracket shows the number of equivalent bonds. Adapted from ref. [41].	13
1.7	(a) The crystal structure of the $\text{Na}_3\text{V}_2(\text{PO}_4)_3$ (NVP), synthesized by solid-state route, in a standard orientation where the magenta and dark green balls denote the Na1 and Na2 atoms, respectively, peach color denotes oxygen atoms, royal blue and purple correspond to P and V atoms, respectively, as visualized with the VESTA software; (b) Rietveld refined XRD Pattern of NVP, synthesized by the solid state route, (c) Raman spectrum of the NVP measured at $\lambda = 514$ nm at room temperature; (d) The CV profile and (e) the electrochemical performance (rate capability) of NVP at different rates; (f) In-situ XRD Patterns of NVP cycled between 2.7 and 3.7 V at 0.1 C rate, Adapted from ref. [58].	15

1.8	(a) The crystal structure of the $\text{Na}_3\text{V}_2(\text{PO}_4)_2\text{F}_3$ (NVPF) [81]; (b) the CV plot of NVPF at a scan rate of 0.5 mV/s for different cycles [83]; (c) In-operando XRD Pattern of NVPF [89]; (d) the crystal structure of $\text{Na}_3\text{V}_2\text{O}_y(\text{PO}_4)_2\text{F}_{3-y}$ [92]; (e) Galvanostatic charge/discharge profile of $\text{Na}_3\text{V}_2\text{O}_2(\text{PO}_4)_2\text{F}$ in the voltage range of 1.0-4.5V, with the extraction of three Na-ions [93]; (f) In-situ XRD patterns of $\text{Na}_3\text{V}_2\text{O}_2(\text{PO}_4)_2\text{F}$ during charging and discharging [94]; (g) the rate performance of graphene quantum dots coated $\text{Na}_3\text{V}_2\text{O}_2(\text{PO}_4)_2\text{F}@C$ for 2000 cycles [95]; (h) the structure evolution of the intermediate product of $\text{Na}_3\text{V}_2(\text{PO}_4)_2\text{F}_3$ by annealing [98]. . . . .	17
1.9	(a) The list of characteristic properties of the separators for efficient battery performance, Adapted from ref. [102] and (b) the comparison of anodic interface with and without the ferroelectric fillers in the polymer matrix of the separators. . . . .	22
1.10	A demonstration of the essential properties of the electrolytes in SIBs: Chemical and electrochemical stability in (a) Al current collectors, (b) electrochemical stability window, (c) thermal stability, (d) ionic conductivity and (e) cost-effectiveness, environmentally benign, sustainable resources. Adapted from ref. [119]. . . . .	25
1.11	The conductivity (shown in black bars and Y axis on left hand side) and viscosity (shown in green bars and Y axis on right hand side) for PC-based electrolytes with 1M of various Na salts, shown in (a), for electrolytes based on 1M $\text{NaClO}_4$ dissolved in various solvents and solvent mixtures in (b); (c,d) Electrochemical potential window stability (black bars and upper y axis) and thermal range (green bars and lower y axis) values for electrolyte combinations, mentioned in (a) and (b). Adapted from ref. [123].	26
1.12	The schematic illustration of the sodium-ion battery with the three classes of the solid electrolyte. Adapted from ref. [133]. . . . .	28
1.13	(A) The different types of solid electrolytes, showing ion transport and (b) illustration of ion conduction mechanism in composite polymer solid electrolytes. Adapted from ref. [133]. . . . .	29
1.14	(a) The important properties of the hard carbon as anode in the electrochemical performance; the structure–function correlation: (b,c) the charge storage mechanism in the hard carbon electrode during battery operation. The panel (b) is adapted from ref. [141]. . . . .	31
2.1	(a) The schematic representation of the ball-milling assisted solid-state mixing, followed by high temperature annealing; (b) the photographs of the ball-milling instrument, vacuum oven and high temperature tube furnace (from left to right). . . . .	58
2.2	The schematic representation of the sol to gel formation process and high temperature annealing process in a tube furnace in an Ar environment. . . . .	60
2.3	The schematic representation of preparation of composite polymer solid electrolyte films through solution-casting method. . . . .	62
2.4	An illustration depicting electron-matter interaction. . . . .	63
2.5	(a) The schematic demonstration of the FESEM instrument; (b) the photograph of the FESEM instrument and (c) the zoomed view of the sample stage (dashed region (b)) with the inset showing the sample mounted on aluminum stub. . . . .	64

2.6	(a) The schematic demonstration of the HR-TEM instrument; (b) the photograph of the HR-TEM instrument and (c,d) zoomed view of sample stage input with single tilt holder and vacuum control system. . . . .	65
2.7	(a) The Raman effect, depicting Rayleigh, Stokes and Anti-stokes Scattering; (b) the photograph of Raman spectrometer. . . . .	67
2.8	(a) The schematic demonstration of the FT-IR instrument; (b) the photograph of the FT-IR instrument. . . . .	68
2.9	(a) The schematic demonstration of emission spectrometer; (b) the photograph of ICP-OES instrument. . . . .	70
2.10	(a) An illustration of Bragg's law; (b) the photograph of tabletop XRD instrument and (c) an electrochemical cell for the operando measurements alongwith the schematic representation of components; (d) an actual picture of the sample stage with the X-ray source (I), sample holder (II) and detector (III). . . . .	72
2.11	(a) The real image of the synchrotron X-ray diffractometer with Mythen 24 at TPS 19A beamline; (b) mounting of the powder sample into capillaries and on sample stage (inset); (c) the photograph of the capillary containing powder sample and its zoomed region of interest in inset. The panels (a) and (c) are adapted from ref. [22]. . . . .	73
2.12	(a) The schematic depicting the ejection of core level electron on the absorption of X-ray photons; (b) an illustration of the XPS instrument setup; (c,d) the photograph of XPS instrument with the sample input stage in panel (c). . . . .	75
2.13	(a) The schematic demonstration of <i>in-situ/operando</i> TXM experiment, Adapted from ref. [26] ; (b) the photograph of sample mounting stage at the TLS 01B1 beamline. Adapted from ref. [27] . . . . .	76
2.14	The real images demonstrating the slurry preparation, electrode fabrication and coin cell assembly protocols. . . . .	78
2.15	(a) The GCD profiles at low and high current densities; (b) the potential and current dependence profile, illustrating the different polarization regions. . . . .	80
2.16	(a) The GITT curve containing series of pulses during the discharge, (b) a single galvanostatic titration pulse demonstrating the $\Delta E_\tau$ and $\Delta E_s$ ; (c) a Nyquist plot ( $-Z''(\Omega)$ versus $Z'(\Omega)$ ) in the low to high frequency region, (d) the $Z'$ versus frequency plot and Randle's equivalent circuit in the inset. . . . .	83
2.17	(a) An illustration of a typical CV curve with a redox couple; (b) the CV profiles at different scan rates. . . . .	88
2.18	A schematic illustration of the different charge storage mechanisms (Faradaic, Pseudocapacitive and supercapacitor; left to right in first row), probed through the CV measurements. The second row shows corresponding CV profiles to each of charge storage mechanism. The third row depicts the current-scan rate dependence and units. The pink circles represent the host ions and the teal rectangle corresponds to the host lattice, while the teal circles represent adsorbed ions. . . . .	90
3.1	The schematic illustration of synthesis procedure for the $\text{Na}_3\text{V}_{2-x}\text{Co}_x(\text{PO}_4)_3/\text{C}$ ( $x = 0, 0.05, 0.10, 0.15$ ) samples. . . . .	100

- 3.2 The powder X-ray diffraction (XRD) patterns (red), the Rietveld refined profiles (black), the fitting residue (blue) and the Bragg positions (green bars) (a-d) and (e) the Synchrotron XRD patterns for the  $\text{Na}_3\text{V}_{2-x}\text{Co}_x(\text{PO}_4)_3$  ( $x = 0, 0.05, 0.1, 0.15$ ) samples. (f) The magnified Synchrotron XRD pattern of  $\text{Na}_3\text{V}_{2-x}\text{Co}_x(\text{PO}_4)_3$  in the  $2\theta$  range of  $31.25 - 32.39^\circ$  and (g) the crystal structure of NVP-Co5 sample where V, Na1, Na2, P, O, C, Co are depicted by the magenta, pink, purple, orange, yellow and blue, drawn using the VESTA software. . . . . 101
- 3.3 The FE-SEM image of the NVP and NVP-Co5 sample (a, b); the EDS mapping of all the elements in NVP-Co5 in (c-h); the HR-TEM diffraction fringes and SAED pattern for NVP (i-j) and NVP-Co5 (k-l), respectively. 104
- 3.4 The Raman spectra (a) and the FTIR spectra (b); the Na/V ratio from the ICP-OES results (c) for the  $\text{Na}_3\text{V}_{2-x}\text{Co}_x(\text{PO}_4)_3/\text{C}$  ( $x = 0, 0.05, 0.1, 0.15$ ) powder samples; The V  $2p$  core level spectra for the NVP (d) and NVP-Co5 (e) powder samples. The Na  $1s$  core level spectra of the NVP (f) and NVP-Co5 (g) powder samples, respectively. . . . . 106
- 3.5 (a-d) The galvanostatic charge-discharge characteristics at the different C-rates for the  $\text{Na}_3\text{V}_{2-x}\text{Co}_x(\text{PO}_4)_3/\text{C}$  ( $x = 0, 0.05, 0.1, 0.15$ ) electrodes. . 108
- 3.6 (a) The rate capability at the different current rates for  $\text{Na}_3\text{V}_{2-x}\text{Co}_x(\text{PO}_4)_3/\text{C}$  ( $x = 0, 0.05, 0.1, 0.15$ ) composites. The specific capacity and the Coulombic efficiency of all the cathode materials for the long cycle performance at the (b) 0.5 C for 200 cycles and (c) 10 C rates for 500 cycles, respectively. In (c) the long cycling data are also presented for another cell of best performing electrode (NVP-Co5) up to 1500 cycles. . . . . 109
- 3.7 The CV curves at different scan rates for the  $\text{Na}_3\text{V}_{2-x}\text{Co}_x(\text{PO}_4)_3/\text{C}$  ( $x = 0, 0.05, 0.1, 0.15$ ) electrodes (inset shows the zoomed view of redox couple,  $\text{V}^{4+}/\text{V}^{5+}$ ). . . . . 111
- 3.8 The cyclic voltammogram at scan rates from 0.1 - 1.0 mV/s, the peak current versus scan rate, the log of the peak current versus log of scan rates, and the contribution of the capacitive and diffusive components from the total current at all scan rates, for the NVP (a-d) and NVP-Co5 (e-h) cathodes, respectively. . . . . 112
- 3.9 (a) The Nyquist Plots ( $-Z''$  vs.  $Z'$ ) measured after three cycles of charge-discharge at 0.1 C rate and (b) the  $Z'$  versus frequency plots for the  $\text{Na}_3\text{V}_{2-x}\text{Co}_x(\text{PO}_4)_3/\text{C}$  ( $x = 0, 0.05, 0.1, 0.15$ ) electrodes. The single titration curve for (c) charging and (d) discharging, and the GITT profiles for the charge (e, g) and discharge (f, h) curves, along with their corresponding diffusion coefficient values for the NVP-Co5 and NVP electrodes, respectively. . . . . 115
- 3.10 The galvanostatic charge-discharge (GCD) profiles of the full cells at 0.1 C rate for initial five cycles for the  $\text{Na}_3\text{V}_{2-x}\text{Co}_x(\text{PO}_4)_3/\text{C}$  ( $x = 0, 0.05, 0.1, 0.15$ ) cathodes with the presodiated hard carbon anode at room temperature 117
- 3.11 (a) The *ex-situ* XRD patterns, and the SEM micrographs for the pristine electrode (b), the cycled electrode at 0.5 C rate for 200 cycles (c), and 10 C rate for 500 cycles (d) for the NVP-Co5 sample. The *ex-situ* XPS core-level spectra of the (e) V  $2p$ , (f) Na  $1s$ , (g) P  $2p$  and (h) O  $1s$  for the charged (4.3 V) state of the NVP-Co5 electrode. . . . . 118

4.1	(a, b) The synchrotron X-ray diffraction patterns of the $\text{Na}_3\text{V}_{2-x}\text{Ni}_x(\text{PO}_4)_2\text{F}_3/\text{C}$ ( $x = 0, 0.05$ )/C powders with rietveld refined profiles; (c) the crystal structure of the NVPF with the $\text{Ni}^{2+}$ substituted at the $\text{V}^{3+}$ site, where the Na1, Na2, V, Ni, P, O, F are shown by the yellow, mixed yellow-white, teal, blue, dark purple, light pink and light green colors; the high resolution FE-SEM image for the (d) $x = 0$ and (e) $x = 0.05$ with its zoomed view at 10 KX in (f); the high resolution TEM images for the $x = 0.05$ , showing particles and carbon coating (cuboid-like particle in inset) in (g), and corresponding diffraction gratings with $d$ -spacing calculations and FFT (inset) in (h) and the SAED pattern (i) with the corresponding surface profile in inset.	133
4.2	(a–e) The powder X-ray diffraction patterns of the $\text{Na}_3\text{V}_{2-x}\text{Ni}_x(\text{PO}_4)_2\text{F}_3$ ( $x = 0–0.07$ )/C powder samples with the Rietveld refined profiles, Bragg positions as well as residual profiles.	134
4.3	(a) The elemental mapping of the elements (Na, V, Ni, P, O, F) for the $x = 0.05$ sample and the corresponding EDX compositions in (b) through HAADF–STEM measurements; the HR–TEM measurement of $x = 0$ sample highlighting the particle in the inset of (c) showing carbon coating, (d) the SAED pattern with the lattice fringes; the SEM images of (e) $x = 0.01$ , (f) $x = 0.03$ and (g) $x = 0.07$ samples.	136
4.4	(a) The FTIR and (b) Raman spectrum for the $\text{Na}_3\text{V}_{2-x}\text{Ni}_x(\text{PO}_4)_2\text{F}_3/\text{C}$ ( $x = 0, 0.01, 0.03, 0.05, 0.07$ )/C samples; (c) the XPS survey scan for the $x = 0$ and $x = 0.05$ samples; the core level spectra of the $x = 0$ in (d) Na 1s, (e) F 1s, (f) V 2p, (g) P 2p and (l) C 1s, and for the $x = 0.05$ in (h) Na 1s, (i) F 1s, (j) V 2p, (k) P 2p, (m) C 1s and (n) Ni 2p.	138
4.5	(a–e) The galvanostatic charge-discharge (GCD) characteristics at the different C-rates (0.1–10 C) for the $\text{Na}_3\text{V}_{2-x}\text{Ni}_x(\text{PO}_4)_2\text{F}_3/\text{C}$ ( $x = 0–0.07$ ) cathodes. (f) the comparison of GCD profiles measured at 0.1 C.	140
4.6	(a) The rate performance at different C rates, the long cyclic performance (b) at 0.5 C rate up to 300 cycles for the $\text{Na}_3\text{V}_{2-x}\text{Ni}_x(\text{PO}_4)_2\text{F}_3/\text{C}$ ( $x = 0–0.07$ ) cathodes, and (c) at 10 C rate up to 2000 cycles for the $x = 0.05$ .	141
4.7	(a–c) The cyclic voltammogram at different scan rates for the $\text{Na}_3\text{V}_{2-x}\text{Ni}_x(\text{PO}_4)_2\text{F}_3/\text{C}$ ( $x = 0.01, 0.03, 0.07$ )/C cathodes; (d) the $Z'$ versus $\omega^{-0.5}$ plot for all the cathodes; (e) the schematic of ion-blocking configuration; (f) the bar graph for the conductivity of $\text{Na}_3\text{V}_{2-x}\text{Ni}_x(\text{PO}_4)_2\text{F}_3/\text{C}$ ( $x = 0, 0.01, 0.03, 0.05, 0.07$ ) samples through ion blocking method.	143
4.8	The cyclic voltammogram (CV) at scan rates from 0.1–1.0 $\text{mVs}^{-1}$ , the peak current versus scan rate, the log of peak current versus log of scan rates, and the contribution of the capacitive and diffusive components from the total current at different scan rates, for the pristine (a–d) and $x = 0.05$ (e–h) cathodes, respectively; the GITT profiles and the diffusion coefficients during the charging and discharging measured at 0.1 C rate in the 2.0–4.5 V range for the (i) pristine and (j) $x = 0.05$ cathodes, (k) the Nyquist Plot (Re Z vs -ImZ) for all the cathodes ( $x = 0–0.07$ ) with Randles circuit in the inset.	145

4.9	(a) The contour 2D plot of the <i>operando</i> XRD experiment, (b) the galvanostatic charge and discharge curves for first cycle charge–discharge, second cycle charge–discharge and third cycle charge, the variation of (c) the lattice parameters ( $a$ and $c$ ) and (d) the cell volume ( $V$ ) during the sodiation and desodiation process; (e) the recorded XRD patterns on the $x = 0.05$ cathode while charging (denoted as c) and discharging (denoted as d) at 0.3 C rate with the step size of $0.03^\circ$ alongwith the zoomed view of (111, 220, 222) diffraction peaks in (f–h). . . . .	148
4.10	(a) The GCD profile of the <i>in-situ</i> TXM measurement at 1 C after cell formation for the $x = 0.05$ cathode, (b, c) the mosaic patterns of the electrode at two regions showing particles (A, B, C); (d, e) the mosaic pattern during the charging and discharging (f, g) for the selected regions shown in panel (b, c), recorded after 60s during the charging and discharging process. . . . .	150
4.11	The <i>in-situ</i> synchrotron TXM images of the selected particle, A for $x = 0.05$ cathode; particle B at OCV (j), charge (k, l) and discharge (m); snapshots of a single particle, during the charge (n, red outline) and discharge (o, blue outline) at different potentials (all at a scale of $2.5\mu\text{m}$ ). . . . .	151
4.12	The KK–residuals (%), obtained for both the real and imaginary parts of impedance for (a) formation cycle, (b) 10, (c) 30, (d) 60, (e) 90, (f) 100, (g) 120 and (h) 150 cycles for the $x = 0.05$ cathode and (i) the Na  Na symmetric cell with the Ni5  Ni5 symmetric cell in the inset. . . . .	153
4.13	(a) The <i>in-situ</i> Nyquist plots recorded at 0.5 C for the $x = 0.05$ cathode up to 150 cycles after the formation process; the DRT profiles with cycle life: (b) at selected cycles, (c) fresh cell (inset shows the formation process), (d) 10 <sup>th</sup> cycle, (e) 30 <sup>th</sup> cycle, (f) 60 <sup>th</sup> cycle, (g) 90 <sup>th</sup> cycle, (h) 100 <sup>th</sup> cycle, (i) 120 <sup>th</sup> cycle, (j) 150 <sup>th</sup> cycle, (k) Ni5  Ni5 and (l) Na  Na symmetric cells. . . . .	154
4.14	The post–mortem study for $\text{Na}_3\text{V}_{2-x}\text{Ni}_x(\text{PO}_4)_2\text{F}_3/\text{C}$ ( $x = 0, 0.01, 0.03, 0.05, 0.07$ ) electrodes: (a) the XRD patterns; SEM micrographs collected at 5 keV after 300 cycles at 0.5 C (b–f); the high resolution SEM image for the $x = 0.05$ cycled electrode measured at 15 keV. . . . .	156
5.1	Design of the full cell configuration, employing the trilayer ceramic–polymer impregnated cellulose paper separators sandwiched between the NVP and HC electrodes. . . . .	168
5.2	(a) The x-ray diffraction patterns of the S050, S075 and S100 paper separators, and (b) the ATR-FTIR spectra for all the separators (glass fiber, S050, S075 and S100). (c) the zoomed view between $500\text{--}1500\text{ cm}^{-1}$ ; (d) the x-ray diffraction pattern of the commercial glass fiber separator (GBR-100). . . . .	171
5.3	The FE-SEM images for the S075 paper separator and the corresponding elemental mappings in the selected regions in (a) and (h) for the top surface (a–g) and bottom surface (h–n), respectively. . . . .	172
5.4	The FE-SEM images of the commercial glass fiber separator with the scale of (a) $10\ \mu\text{m}$ , (b) $2\ \mu\text{m}$ and (c–e) the corresponding elemental mapping over the selected region, as in (a). . . . .	173

- 5.5 The electrolyte soaking ability test for the paper separators S050 (i), S075 (ii) and S100 (iii), soaked in the liquid electrolyte for (a) 0 hrs and (b) 2 hrs; (c-e) the digital photographs of the paper separator, S075 at various stages of folding and bending, (f) the digital photograph of the folded region of the S075 separator taken for the FE-SEM measurement, (g) the FE-SEM images of the S075 separator on the folded region at the magnification of 500x, the bottom surface of the folded area at the magnification of (h) 5000x and (i) 10000x, the top surface of the folded area with (j) 5000x and (k) 10000x. . . . . 174
- 5.6 (a) The variation of Gurley values of untreated paper substrate (PS) and the developed separators (P35S35B20S050, P35S35B20S075 and P35S35B20S100), (b) The stress versus strain plots of the developed paper separators in machine direction (MD) as well as in transverse direction (TD). . . . . 175
- 5.7 The qualitative thermal shrinkage measurement of the developed paper separators at 25°C and 200°C. . . . . 176
- 5.8 The Barrett-Joyner-Halenda (BJH) plots of the developed paper separators. 177
- 5.9 (a) The FE-SEM image of the folded region of the S075 separator, and (b-f) the corresponding elemental mappings (O, C, Ba, Ti) for the selected region of the folded part. . . . . 178
- 5.10 (a) The Nyquist plot for all the separators at the room temperature; (b) the Nyquist plot for the control, S075 membrane at the various temperatures (27°C, 30°C, 35°C, 40°C, 45°C, 50°C, 55°C), using a blocking electrode system (SS||Separator||SS); (c) the ionic conductivity values for the S075 separator at the different temperatures. . . . . 179
- 5.11 The electrochemical characterisation of HC anode: (a) The Nyquist impedance spectra and the inset shows the zoomed semicircle, depicting the charge transfer resistance; (b) the galvanostatic charge-discharge profiles at various current densities; (c) the cycle life and coulombic efficiency at 0.1 A g<sup>-1</sup> for 110 cycles; (d) the rate performance at the different current densities (five cycles each); the CV curves for the first three cycles at the scan rate of 0.05 mV s<sup>-1</sup> (e) and (f) different current densities (0.05–1 mV s<sup>-1</sup>); (g) the peak current vs. scan rate; (h) log of the peak current vs. log of scan rates; (i) the contribution of the capacitive and diffusive components from the total current at all scan rates. . . . . 181
- 5.12 The electrochemical performance of the S050, S075, S100 and glass fiber separator based full cell system: (a–d) the galvanostatic charge-discharge profiles; (e) the mechanism for the functioning of separators; (f) the rate performance at the different C rates; (g-j) the cycle life and Coulombic efficiency at 0.5 C rate between 41 and 240 cycles (cycle life is measured after the rate performance is finished in 40 cycles for the same set of cells). 183
- 5.13 (a–d) The Nyquist plots for the NVP-HC full cells with glass fiber, and paper separator (S050, S075 and S100) for the fresh and after stabilizing the SEI at 0.1 C for five cycles, along with the fitting using Randles circuit shown in the insets. . . . . 184
- 5.14 The CV curves at the different scan rates (0.05–1.0 mV s<sup>-1</sup>) and (b) the GITT measurements at a current rate of 0.3 C in the potential window of 2.0–4.3V for the NVP cathode using the S075 separator with HC anode in the full cell configuration. . . . . 188

5.15	(a-f) The Nyquist plots for the aged NVP-HC full cells using S075 paper separator for 0, 1, 2, 3, 4 and 5 weeks. . . . .	188
6.1	The material characterization of as prepared $\text{Na}_3\text{Zr}_2\text{Si}_2\text{PO}_{12}$ ceramic material: (a) Rietveld refined XRD pattern; (b) the crystal structure, drawn with VESTA; (c) the molar concentration of elements, obtained from ICP-OES; (d) DLS spectra for particle size distribution; (e) the high resolution FE-SEM image at a scale of 1 $\mu\text{m}$ and 500 nm (inset); the elemental mappings of elements of NZSP across a selected region (f); (g) the HR-TEM image with zoomed image (inset); (h) diffraction fringes; (i) SAED pattern; the XPS core level peaks (j) Na 1s, (k) Zr 3d, (l) P 2p and (m) Si 2p. . . . .	204
6.2	(a) The schematic for the preparation of ionic liquids and ceramic filler composite polymer electrolyte films; the real photographs of the composite polymer solid electrolyte membranes at different stages: (b) flat, (c) folded, (d) bent and (e) flat after folding and bending; (f) XRD pattern and (g) ATR-FTIR pattern for all electrolyte films. . . . .	206
6.3	The photoemission spectra of CPE membranes with different plasticizers: the core levels C 1s, F 1s, O 1s, S 2p and N 1s in (a1-e1) NZSP; (a2-e2) PMPFSI; (a3-e3) PMPTFSI; (a4-e4) EMIFSI and (a5-e5) SCN, respectively. . . . .	207
6.4	The high resolution cross-section FE-SEM images of CPE membranes with different plasticizers: (a1-a3) NZSP; (b1-b3) PMPFSI; (c1-c3) PMPTFSI; (d1-d3) EMIFSI and (e1-e3) SCN at different magnifications. . . . .	209
6.5	The high resolution FE-SEM surface image for the (a-c) NZSP and (d-f) EMIFSI films at different magnifications; the elemental distribution of elements over selected region (d) for EMIFSI film (g-l). . . . .	210
6.6	(a) The room temperature LSV plots of the Na//EMIFSI//SS and Na//NZSP//SS cell configuration; (b) the impedance spectra of the symmetric cells (SS//CPE//SS) for all the fabricated CPEs. . . . .	211
6.7	The galvanostatic charge and discharge profiles at the different C-rates with plasticizer as (a) pristine $\text{Na}_3\text{Zr}_2\text{Si}_2\text{PO}_{12}$ , (b) N-propyl-N-methylpyrrolidinium bis(fluorosulfonyl)imide, (c) 1-Ethyl-3-methylimidazolium bis(fluorosulfonyl)imide, (d) Succinonitrile, (e) N-propyl-N-methylpyrrolidinium bis(trifluoromethanesulfonyl)imide and (f) all the CPEs at 2 C rate; (g) the cycle life performance for the plasticized CPEs at 0.5 C rate for 150 cycles. . . . .	213

# List of Tables

1.1	Characteristics of Li, Na and K as charge carriers, taken from [10] and [11]	5
3.1	The XRD analysis parameters for the $\text{Na}_3\text{V}_{2-x}\text{Co}_x(\text{PO}_4)_3/\text{C}$ ( $x = 0, 0.05, 0.1, 0.15$ ) samples.	103
3.2	The ICP-OES results for the $\text{Na}_3\text{V}_{2-x}\text{Co}_x(\text{PO}_4)_3/\text{C}$ samples, described in molar ratio.	106
3.3	Comparison of the electrochemical performances (current rate, discharge capacity, number of cycles, capacity retention) of the NVP electrode modified with the element substitutions.	112
4.1	X-ray diffraction analysis results for the $\text{Na}_3\text{V}_{2-x}\text{Ni}_x(\text{PO}_4)_2\text{F}_3/\text{C}$ ( $x = 0, 0.01, 0.03, 0.05$ and $0.07$ ) samples.	137
4.2	The anodic and cathodic potentials and peak differences from the CV measurement at a scan rate of $0.1 \text{ mV s}^{-1}$ for the $\text{Na}_3\text{V}_{2-x}\text{Ni}_x(\text{PO}_4)_2\text{F}_3/\text{C}$ ( $x = 0, 0.01, 0.03, 0.05, 0.07$ ) samples.	144
4.3	The polarization values ( $\Omega$ ) for the different components of the EIS spectra with evolution of cycle life, obtained from the DRT analysis of the optimized $x = 0.05$ cathode.	155
5.1	The comparison of the thickness, air permeability, pore characteristics, and Young's Modulus along with the MD and TD direction of the developed paper separators.	173
5.2	The summary of the tensile properties of the developed paper separators.	177
5.3	The resistance and bulk conductivity values for all the developed paper separators and temperature-dependent conductivity values for the S075 separator.	180
5.4	The values of the charge transfer resistance ( $R_{ct}$ ) before and after cycling for $0.1 \text{ C}$ rate for the 5 cycles for the interface stabilisation for all the separators.	186